

# Strong magnetic fields: neutron stars with an extended inner crust

Helena Pais<sup>1</sup>, Bruno Bertolino<sup>1</sup>, Jianjun Fang<sup>2</sup>, Xiaopeng Wang<sup>2</sup>, and Constança Providência<sup>1</sup>

<sup>1</sup> CFisUC, Department of Physics, University of Coimbra, 3004-516 Coimbra, Portugal.

<sup>2</sup> School of Physics and Physical Engineering, Qufu Normal University, 273165 Qufu, China.

Received: date / Revised version: date

**Abstract.** Using relativistic mean-field models, the formation of clusterized matter, as the one expected to exist in the inner crust of neutron stars, is determined under the effect of strong magnetic fields. As already predicted from a calculation of the unstable modes resulting from density fluctuations at subsaturation densities, we confirm in the present work that for magnetic field intensities of the order of  $\approx 5 \times 10^{16}$  G to  $5 \times 10^{17}$  G, pasta phases may occur for densities well above the zero-field crust-core transition density. This confirms that the extension of the crust may be larger than expected. It is also verified that the equilibrium structure of the clusterized matter is very sensitive to the intensity of the magnetic fields. As a result, the decay of the magnetic field may give rise to internal stresses which may result on the yield and fracture of the inner crust lattice.

**PACS.** XX.XX.XX No PACS code given

## 1 Introduction

Neutron stars are compact objects with a very complex structure. Their interior is generally divided into an outer and inner crust and an outer and inner core. The information coming to the surface from the interior of the star will necessarily cross the crust, and, therefore, it is essential to know well the constitution of the crust not only because of the processes that result directly from the crust but also in order to learn about the core of the star. The inner crust that lies directly at the border with the core has a complex constitution. In particular, it is generally accepted that the layers just below the crust-core transition are formed by frustrated matter resulting from the competition between the strong and the electromagnetic interactions [1,2,3,4,5,6,7,8,9]. Neutron star phenomena that seem to be directly related with the properties of the inner crust are glitches [10,11,12] or the evolution of the magnetic field intensity [13]. Neutron superfluidity in the inner crust plays an essential role in the interpretation of the glitches [10], but the entrainment of neutrons to the solid crust may raise some problems on whether the description of glitches is totally described by the crust [11,12]. In [13], the authors have shown that the dissipation of the magnetic field responsible for a fast spin down of the stars could be a signal of the presence of a highly resistive layer of matter in the inner crust, and that the existence of pasta phases as suggested in [1], were a possibility.

A class of neutron stars known as magnetars is characterized by very intense surface magnetic fields which span the range  $\sim 10^{12-15}$  G [14,15]. Inside these stars the magnetic field could be even more intense, and several estimates and simulations suggest that fields of the order of  $\sim 10^{18}$  G could exist in their interior [16,17,18,19,20,21].

In the present study, we want to calculate the structure of the bottom layers of the inner crust in the presence of a strong magnetic field. It has been reported that the extension of the inner crust under these conditions could be much larger, and it could have a complex structure constituted by alternating regions of clusterized and non-clusterized matter above the  $B = 0$  crust-core transition [22,23,24,25], defining a transition region with a finite width.

The extension of the crust in a neutron star is directly connected to the presence of a liquid-gas type transition in nuclear matter [26]. In Refs. [22,23], the effect of a strong magnetic field on the density that characterizes the transition to homogeneous matter was determined within the framework of the dynamical spinodal, i.e. the surface that limits the region where nuclear matter is unstable with respect to density fluctuations as defined in [27]. This method had been applied to the study of the fragmentation of a finite nuclear system within a self-consistent quantum approach in Refs. [28,29].

Results in [22,23] indicate that the region defined by the  $B = 0$  spinodal section is not much affected for finite  $B \lesssim 10^{17}$ G. However, besides this main region of instability, other unstable regions were identified at larger densities. The same conclusion was drawn within a ther-

*Correspondence to:* Helena Pais, [hpais@uc.pt](mailto:hpais@uc.pt), Constança Providência, [cp@uc.pt](mailto:cp@uc.pt)

modynamical spinodal approach [24,25,30]. One expects that pasta configurations will emerge at these densities, and this is the main objective of the present work: to investigate the possible extension of the nonhomogeneous matter region and the existence of islands of clusterized matter above the  $B = 0$  crust-core transition.

In Refs. [31,32], the effect of strong magnetic fields on the inner crust constitution has been studied using a Thomas-Fermi approach. However, the magnetic field intensities considered were generally quite high, and the region above the  $B = 0$  crust-core transition was not investigated. According to Ref. [21], the neutral line of a poloidal magnetic field may fall inside the extended non-homogeneous region. The existence of these regions may be important to avoid the development of magnetic field instabilities [33].

The crust-core transition density depends on the properties of the nuclear equation of state, in particular, on its symmetry energy, as discussed in several works [34,35,36,37,38,39,40]. This has led us to consider two models with the same isoscalar properties but different isovector ones, in order to determine differences associated with the density dependence of the symmetry energy. In particular, *ab-initio* chiral effective field theory calculations and several experimental nuclear properties seem to favor a small slope of the symmetry energy at saturation,  $L \lesssim 60$  MeV [41]. However, if astrophysical observations are also considered, larger slopes are predicted [42], but still below 90 MeV. Recently, however, the measurement of the skin thickness of  $^{208}\text{Pb}$  [43] seems to indicate that values of the slope  $L$  in the interval  $106 \pm 37$  MeV are expected [44], although not all studies estimate so large values, see [45,46]. A large value of  $L$  is also compatible with the estimate obtained from charged pion spectra measured at high transverse momenta where  $42 < L < 117$  MeV was obtained [47].

The structure of the paper is as follows: after the Introduction, we briefly review the formalism used to determine the equation of state of magnetized matter in Sec. 2, and in Sec. 3, clusterized matter is determined from the Gibbs conditions supplemented by Coulomb and finite size effects. In Sec. 4, the main results are discussed, and in the last section, some conclusions are drawn.

## 2 Magnetized nuclear matter

In the present study we describe clusterized stellar matter under the effect of strong magnetic fields within a nuclear relativistic mean-field (RMF) approach [48,49]. In the following, we also discuss the effect of the anomalous magnetic moment (AMM) on the extension of the clusterized phase.

In the RMF approach, nucleons with mass  $M$  interact with and through the exchange of three different mesonic fields, an isoscalar-scalar field  $\phi$  with mass  $m_\sigma$  and coupling constant  $g_\sigma$ , an isoscalar-vector field  $V^\mu$  with mass  $m_v$  and coupling constant  $g_v$ , and an isovector-vector field  $\mathbf{b}^\mu$  with mass  $m_\rho$  and coupling constant  $g_\rho$ . In order to describe electrically neutral matter, electrons will also be con-

sidered explicitly. The charged particles interact through the static electromagnetic field  $A^\mu$ ,  $A^\mu = (0, 0, Bx, 0)$ , so that  $\mathbf{B} = B \hat{z}$  and  $\nabla \cdot \mathbf{A} = 0$ . In the present study, we consider that i) the electromagnetic field is externally generated, ii) field configurations are frozen.

Our system is described by the Lagrangian density:

$$\mathcal{L} = \sum_{i=p,n} \mathcal{L}_i + \mathcal{L}_e + \mathcal{L}_A + \mathcal{L}_\sigma + \mathcal{L}_\omega + \mathcal{L}_\rho + \mathcal{L}_{\omega\rho}, \quad (1)$$

where  $\mathcal{L}_i$  is the nucleon Lagrangian density, given by

$$\mathcal{L}_i = \bar{\psi}_i \left[ \gamma_\mu i D^\mu - M^* - \frac{1}{2} \mu_N \kappa_b \sigma_{\mu\nu} F^{\mu\nu} \right] \psi_i, \quad (2)$$

with

$$M^* = M - g_\sigma \phi, \quad (3)$$

$$i D^\mu = i \partial^\mu - g_v V^\mu - \frac{g_\rho}{2} \boldsymbol{\tau} \cdot \mathbf{b}^\mu - e A^\mu \frac{1 + \tau_3}{2}. \quad (4)$$

The electron Lagrangian density,  $\mathcal{L}_e$  and the electromagnetic term,  $\mathcal{L}_A$ , are defined by

$$\mathcal{L}_e = \bar{\psi}_e [\gamma_\mu (i \partial^\mu + e A^\mu) - m_e] \psi_e, \quad (5)$$

$$\mathcal{L}_A = -\frac{1}{4} F_{\mu\nu} F^{\mu\nu}. \quad (6)$$

We consider  $c = \hbar = 1$ , the electromagnetic coupling constant is  $e = \sqrt{4\pi/137}$ , and  $\tau_3 = \pm 1$  is the isospin projection for protons and neutrons, respectively.  $M^*$  is the nucleon effective mass, and  $m_e$  the electron mass. The inclusion of the AMM is undertaken via the coupling of the nucleons to the electromagnetic field tensor,  $F_{\mu\nu} = \partial_\mu A_\nu - \partial_\nu A_\mu$ , with  $\sigma_{\mu\nu} = \frac{i}{2} [\gamma_\mu, \gamma_\nu]$ , and strength  $\kappa_b$ , with  $\kappa_n = -1.91315$  for the neutron,  $\kappa_p = 1.79285$  for the proton, and  $\mu_N$  the nuclear magneton. It was discussed in [50], that the contribution of the AMM of electrons is negligible and, therefore, it will not be included. Notice that medium effects may affect the AMM, as it was shown, for instance, in [51]. In the present study, we consider the vacuum values.

The mesonic Lagrangians are given by

$$\begin{aligned} \mathcal{L}_\sigma &= \frac{1}{2} \left( \partial_\mu \phi \partial^\mu \phi - m_\sigma^2 \phi^2 - \frac{1}{3} \kappa \phi^3 - \frac{1}{12} \lambda \phi^4 \right), \\ \mathcal{L}_\omega &= -\frac{1}{4} \Omega_{\mu\nu} \Omega^{\mu\nu} + \frac{1}{2} m_v^2 V_\mu V^\mu, \\ \mathcal{L}_\rho &= -\frac{1}{4} \mathbf{B}_{\mu\nu} \cdot \mathbf{B}^{\mu\nu} + \frac{1}{2} m_\rho^2 \mathbf{b}_\mu \cdot \mathbf{b}^\mu, \end{aligned} \quad (7)$$

where  $\Omega_{\mu\nu} = \partial_\mu V_\nu - \partial_\nu V_\mu$ , and  $\mathbf{B}_{\mu\nu} = \partial_\mu \mathbf{b}_\nu - \partial_\nu \mathbf{b}_\mu - g_\rho (\mathbf{b}_\mu \times \mathbf{b}_\nu)$ .  $\kappa$  and  $\lambda$  are the third- and fourth-order parameters of the scalar field.

In order to discuss the effect of the density dependence of the symmetry energy we consider two models, NL3 and NL3 $\omega\rho$ , that have the same isoscalar properties but different isovector properties, as it was considered in [22]. Therefore, we also include in the Lagrangian density the nonlinear term,  $\mathcal{L}_{\omega\rho}$ , that mixes the  $\omega$  and  $\rho$  mesons

$$\mathcal{L}_{\omega\rho} = \Lambda_v g_v^2 g_\rho^2 V_\mu V^\mu \mathbf{b}_\mu \cdot \mathbf{b}^\mu. \quad (8)$$

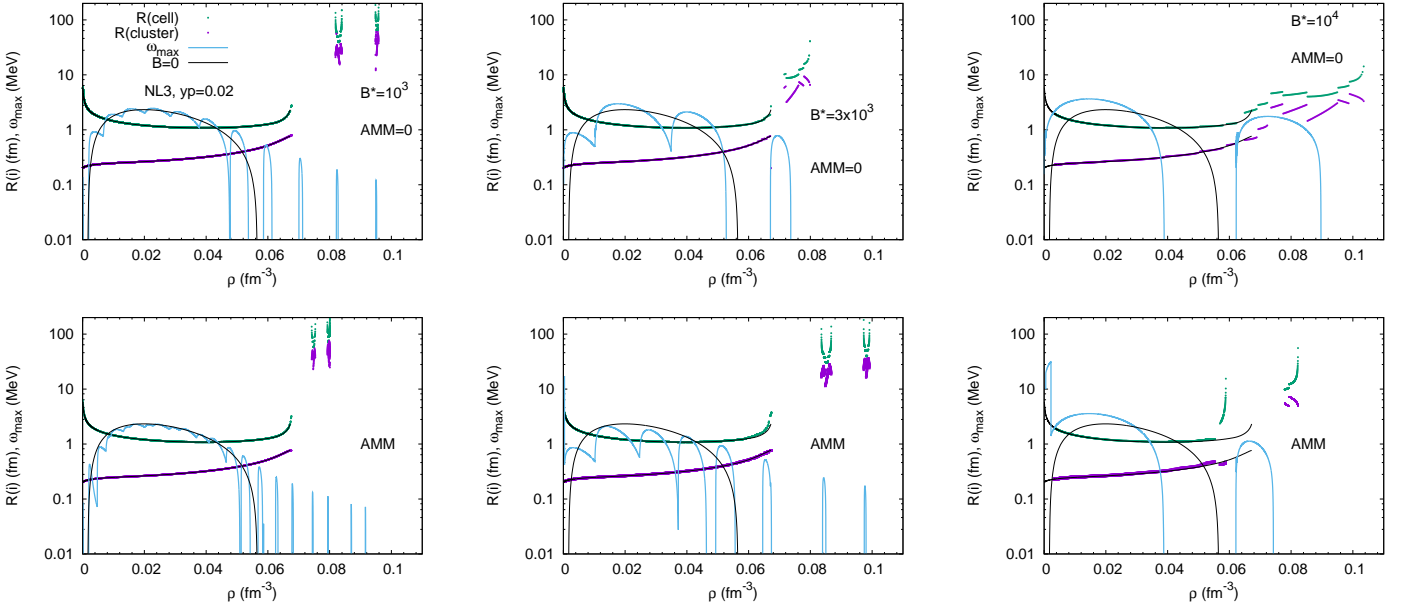


**Fig. 1.** Wigner-Seitz cell (thick green lines) and cluster radii (thick purple lines) ( $R_{WS}$  and  $R_D$ ) and maximum growth rates ( $|\omega|$ ) (thin black solid lines for  $B = 0$  and light blue solid lines for finite  $B$ ) for  $B = 4.4 \times 10^{16} \text{ G}$  (left),  $B = 1.3 \times 10^{17} \text{ G}$  (middle), and  $B = 4.4 \times 10^{17} \text{ G}$  (right) determined for  $y_p = 0.02$  without (top) and with (bottom) AMM for the NL3 model.

This term allows to have a softer symmetry energy than the one of the original NL3 model [52]. This mechanism of modelling the density dependence of the symmetry energy using a non-linear term that mixes the  $\omega$  and  $\rho$  mesons was discussed in [53].

### 3 The pasta phases

In the present study we consider the coexisting phases (CP) method to describe the pasta phases as discussed in [5, 6, 7, 9, 54]. A self-consistent description within a Thomas-Fermi approximation has already been applied to the description of magnetized matter [31, 32]. We will consider such a calculation in a future study since numerical convergence for magnetic field intensities  $\lesssim 5 \times 10^{17} \text{ G}$  is faster within the CP approach we are presently considering. In this approach, the free energy density is minimized considering a mixed phase of dense clusters with different geometrical configurations in a background gas of nucleons and electrons. Finite size effects, as the ones from the cluster surface tension and the Coulomb interaction, are included after the minimization of the free energy.

The free energy density minimum is determined by imposing the Gibbs conditions on the pressure  $P$ , and proton and neutron chemical potentials, respectively  $\mu_p$  and  $\mu_n$ , at the transition from phase I to phase II [5, 6, 7, 9, 54],

$$P^I(E_F^i, M^{*I}) = P^{II}(E_F^i, M^{*II}), \quad i = p, n \quad (9)$$

$$\mu_i^I = \mu_i^{II}, \quad i = p, n. \quad (10)$$

In the above equations, the chemical potentials  $\mu_i$  are given by

$$\mu_p = E_F^p + g_\omega V^0 + \frac{1}{2} g_\rho b^0, \quad (11)$$

$$\mu_n = E_F^n + g_\omega V^0 - \frac{1}{2} g_\rho b^0, \quad (12)$$

with  $E_F^i$  being the effective chemical potentials.

The Gibbs equilibrium conditions are supplemented by the equations that define the nucleon effective masses in both phases,

$$m_\sigma^2 \phi_0^I + \frac{\kappa}{2} \phi_0^{2I} + \frac{\lambda}{6} \phi_0^{3I} = g_\sigma \rho_s^I, \quad (13)$$

$$m_\sigma^2 \phi_0^{II} + \frac{\kappa}{2} \phi_0^{2II} + \frac{\lambda}{6} \phi_0^{3II} = g_\sigma \rho_s^{II}, \quad (14)$$

and by the equation that fixes the global proton fraction

$$f \rho_p^I + (1 - f) \rho_p^{II} = Y_p \rho. \quad (15)$$

In the above equations, I refers to the liquid (cluster) phase and II to the gas phase, and  $f$  is the volume fraction of phase I:

$$f = \frac{\rho - \rho^{II}}{\rho^I - \rho^{II}}. \quad (16)$$

$\rho_s = \rho_{s,p} + \rho_{s,n}$  is the total scalar density with  $\rho_{s,p}$ ,  $\rho_{s,n}$  the proton and neutron scalar densities, respectively, and  $\rho = \rho_p + \rho_n$  is the total nucleonic density, with  $\rho_p$ ,  $\rho_n$  the proton and neutron densities, respectively. They are going to be defined next.  $Y_p$  is the global proton fraction,  $Y_p = \rho_p / \rho$ . We also consider that the density of electrons  $\rho_e$  is uniform in the cell and  $\rho_e = Y_p \rho$ .

The scalar and vector proton and neutron densities in the above equations are defined by [48, 55]

$$\rho_{s,p} = \frac{q_p B M^*}{2\pi^2} \sum_{\nu=0}^{\nu_{\max}} \sum_{\zeta} \frac{\sqrt{M^{*2} + 2\nu q_p B - \zeta \mu_N \kappa_p B}}{\sqrt{M^{*2} + 2\nu q_p B}} \ln \left| \frac{k_{F,\nu,\zeta}^p + E_F^p}{\sqrt{M^{*2} + 2\nu q_p B - \zeta \mu_N \kappa_p B}} \right|, \quad (17)$$

$$\rho_{s,n} = \frac{M^*}{4\pi^2} \sum_{\zeta} \left[ E_F^n k_{F,\zeta}^n - \bar{m}_n^2 \ln \left| \frac{k_{F,\zeta}^n + E_F^n}{\bar{m}_n} \right| \right], \quad (18)$$

$$\rho_p = \frac{q_p B}{2\pi^2} \sum_{\nu=0}^{\nu_{\max}} \sum_{\zeta} k_{F,\nu,\zeta}^p, \quad (19)$$

$$\rho_n = \frac{1}{2\pi^2} \sum_{\zeta} \left[ \frac{1}{3} (k_{F,\zeta}^n)^3 - \frac{1}{2} \zeta \mu_N \kappa_n B \times \left( \bar{m}_n k_{F,\zeta}^n + E_F^n \left( \arcsin \left( \frac{\bar{m}_n}{E_F^n} \right) - \frac{\pi}{2} \right) \right) \right]. \quad (20)$$

In the above equations,  $\kappa_i$ ,  $i = p, n$  are the anomalous magnetic moment strengths, previously defined after Eq. (6).  $k_{F,\nu,\zeta}^p$ ,  $k_{F,\zeta}^n$  are the Fermi momenta of protons and neutrons related to the proton and neutron effective Fermi energies

$$k_{F,\nu,\zeta}^{p2} = E_F^p{}^2 - \left[ \sqrt{M^{*2} + 2\nu q_p B - \zeta \mu_N \kappa_p B} \right]^2, \quad (21)$$

$$k_{F,\zeta}^{n2} = E_F^n{}^2 - \bar{m}_n^2, \quad (22)$$

with  $\bar{m}_n = M^* - \zeta \mu_N \kappa_n B$ .  $\nu = n + \frac{1}{2} - \frac{\zeta}{2} = 0, 1, 2, \dots$  enumerates the quantized Landau levels for protons with charge  $q_p = 1$ , and  $\zeta$  is the spin quantum number, with +1 for spin up and -1 for spin down.

The solution of the equations (9-15) defines the total energy density of the nonhomogeneous matter,

$$\mathcal{E} = f \mathcal{E}^I + (1 - f) \mathcal{E}^{II} + \mathcal{E}_e + \mathcal{E}_{surf} + \mathcal{E}_{Coul}, \quad (23)$$

where  $\mathcal{E}^{I,II}$  refer to the bulk free energy density of phase  $I$  and  $II$ ,  $\mathcal{E}_e$  is the free energy density of an homogeneous electron gas, and the terms  $\mathcal{E}_{surf}$  and  $\mathcal{E}_{Coul}$  were added to take into account, respectively, the surface energy of the clusters and the Coulomb interaction. From the minimization of the sum  $\mathcal{E}_{surf} + \mathcal{E}_{Coul}$  with respect to the size of the cluster, the following relation is obtained [5]  $\mathcal{E}_{surf} = 2\mathcal{E}_{Coul}$ . The Coulomb energy density is defined by [1, 2, 5]

$$\mathcal{E}_{Coul} = \frac{2F}{4^{2/3}} (e^2 \pi \Phi)^{1/3} (\sigma D (\rho_p^I - \rho_p^{II}))^{2/3}, \quad (24)$$

where  $F = f$  is used in the droplet/rod/slab phase and  $F = 1 - f$  for tubes and bubbles,  $\sigma$  is the surface energy coefficient and  $D$  is the dimension of the system. For droplets, rods and slabs, [1, 2]

$$\Phi = \begin{cases} \left( \frac{2-D F^{1-2/D}}{D-2} + F \right) \frac{1}{D+2}, & D = 1, 3; \\ \frac{F-1-\ln(F)}{D+2}, & D = 2. \end{cases} \quad (25)$$

In the present study, we define the surface energy as in Ref. [56], where a parametrization determined within a Thomas-Fermi approach was obtained in terms of the global proton fraction and the temperature,  $\sigma(x, T)$ , with  $x = (1 - 2Y_p)^2$ . Each cluster is considered to be in the center of a charge neutral Wigner-Seitz (WS) cell [5, 57]. The WS cell may have different geometries, and for simplification they are fixed to a sphere, a cylinder, or a slab, and its volume is equal to the one of the unit BCC cell. The dimensions of the WS cell ( $R_{WS}$ ) and of the cluster ( $R_D$ ) are determined from the minimization of the free energy with respect to the cluster dimension  $R_D$  (the radius of the droplet or rod and the thickness of the slab). The following expressions define  $R_D$  and  $R_{WS}$ , see [1, 5]:

$$R_D = \left( \frac{\sigma D}{e^2 (\rho_p^I - \rho_p^{II})^2 \Phi} \right)^{1/3}, \quad (26)$$

$$R_{WS} = \frac{R_D}{F^{1/D}}. \quad (27)$$

## 4 Results

In the following, the nonhomogeneous matter is calculated according to the formalism presented in the previous section. We consider two models that have the same isoscalar properties, but differ on the isovector ones, NL3 [52] and NL3 $\omega\rho$  [39]. The symmetry energy slope at saturation is equal to 118 MeV for NL3 and 55 MeV for NL3 $\omega\rho$ . Recently, an estimation of  $L$  obtained from the measurement of the  $^{208}\text{Pb}$  neutron skin thickness [43] predicts  $106 \pm 37$  MeV [44]. However, other studies based on experimental measurements and ab-initio calculations indicate a much smaller slope,  $L = 51 \pm 11$  MeV [41], or taking into account also astrophysical observations,  $L = 58.7 \pm 28.1$  MeV [42]. The two values of  $L$  we consider represent both scenarios.

It was shown in Ref. [58] that in the lower layers of the inner crust, close to the crust-core transition, the proton fraction does not change much and takes a value close to the one at the transition. For the above models, this corresponds to  $y_p = 0.02$  for NL3 and  $y_p = 0.035$  for NL3 $\omega\rho$ .

In the following, we will study the formation of pasta phases for those proton fractions as an exploratory investigation.

### 4.1 Pasta structures at supra crust-core transition density

We first consider the NL3 model. In Fig. 1, the size of the WS cell  $R_{WS}$  (green points) and the cluster size  $R_D$  (purple points) are plotted together with the growth rate determined within a dynamical spinodal calculation (light blue lines), for magnetic fields with intensities 0.44, 1.3 and  $4.4 \times 10^{17}$  G. This corresponds to  $B^* = 10^3$ ,  $3 \times 10^3$  and  $10^4$ , respectively, because  $B^* = B/B_{ce}$ , with  $B_{ce} = 4.41 \times 10^{13}$  G the critical electron magnetic field. The growth rates have been defined in [23], see Eq. (36), and

are the solutions of the dispersion relation obtained considering fluctuations of the proton, neutron and electron densities. Inside the dynamical spinodal, the solutions of the dispersion relation are imaginary frequencies characteristic of unstable modes. We define the growth rates as the modulus of these solutions. The magnitude of the growth rates depends on the wavelength of the mode, and, for each density we consider the largest growth rate as the one that drives the system. The respective wavelength can be considered an estimation of the size of the clusters formed [59]. Results obtained without (with) the anomalous magnetic moment of the nucleons are shown in the top (bottom) panels. The  $B = 0$  results are represented by thin black lines.

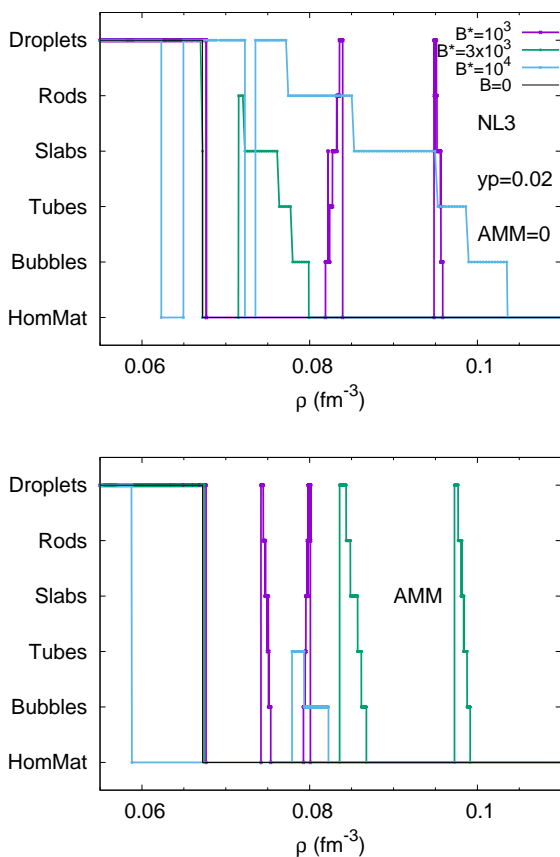


**Fig. 2.** Geometries of the clusters obtained with  $yp=0.02$ , without (top) and with (bottom) AMM within the NL3 model for several magnetic field intensities.

Let us start by analysing the top panels. For the two weaker field intensities represented, the low density region, i.e. the region that is also found in the  $B = 0$  calculations, does not seem to be sensitive to the magnetic field. However, a new feature is present: a region of clustered matter appears at larger densities, of the order of  $0.08-0.09 \text{ fm}^{-3}$ . This region is coincident with a region of instability identified within the dynamical spinodal formalism. For

the magnetic field intensity  $4.4 \times 10^{17} \text{G}$ , the clustered region extends until a density above  $0.1 \text{ fm}^{-3}$ .

In the following, we analyse the effect of including the proton and neutron AMM. Taking as reference the energy  $\epsilon = |\kappa_p + \kappa_n|B \approx 2 \times 10^{-5} B^* \text{ MeV}$ , it is clear that the effect of the AMM is only strong for very strong fields, i.e.  $B^* \gtrsim 10^5$ . However, its effect is seen as soon as the energy difference between different free energy configurations is of the order of  $\epsilon$ . The AMM term gives rise to proton and neutron polarization and, therefore, reduces the softening effect of the Landau quantization on the EoS.

Looking at the bottom panels, the introduction of the AMM in the calculation does not change much the extension of the low density clustered region with respect to the previous situation, but the second region of clustered matter decreases considerably, for the two highest fields considered. In particular, for the strongest field considered, the inclusion of AMM in the calculation results in the division of the clustered region into two disconnected clustered regions separated by homogeneous matter. For this same field, it is also seen that the upper bound of the low density clustered region occurs at smaller densities, when compared to the  $B = 0$  field case [7]. This is in agreement with the results presented in [32], where it is shown that the crust-core transition density decreases for  $B = 10^{18} \text{G}$ , when AMM is taken into account. In our calculation, this decrease is only observed for  $B = 4.4 \times 10^{17} \text{G}$ : the weaker fields do not affect this boundary. Another interesting feature is the fact that for the weaker fields considered, more than two disconnected regions of clustered matter are obtained.

In Fig. 2, we identify the geometry of the clusters obtained within the model NL3 without (top) and with (bottom) AMM. The same magnetic field intensities as before are considered. Some conclusions can immediately be drawn: i) the low density behavior is very similar for the three values of  $B$ . In this region, only droplets are found, consistent with the  $B = 0$  case; ii) a second or more regions of nonhomogeneous matter appear. In the AMM case, and for the two lowest fields considered, two separate regions are found. The same occurs if no AMM is included for the lowest field. In these new regions of clustered matter, all different geometries may occur with an extension and limiting densities very sensitive to the magnetic field. As already discussed, the inclusion of the AMM has also non-negligible effects. For the two highest fields considered, the supra-saturation nonhomogeneous region suffers a shift that depends on the magnetic field intensity considered, and its density extension decreases.

The strong dependence of the structure of these other regions on the magnetic field intensity may have direct effects on the evolution of the magnetar. In fact, the decay of the magnetic field will have consequences on the equilibrium structure of the neutron star and originate internal stresses which may give rise to the yield or the fracture of the lattice.

In the following, we consider the calculation of the non-homogeneous matter within the NL3 $\omega\rho$  model, a model that predicts a much softer density dependence of the

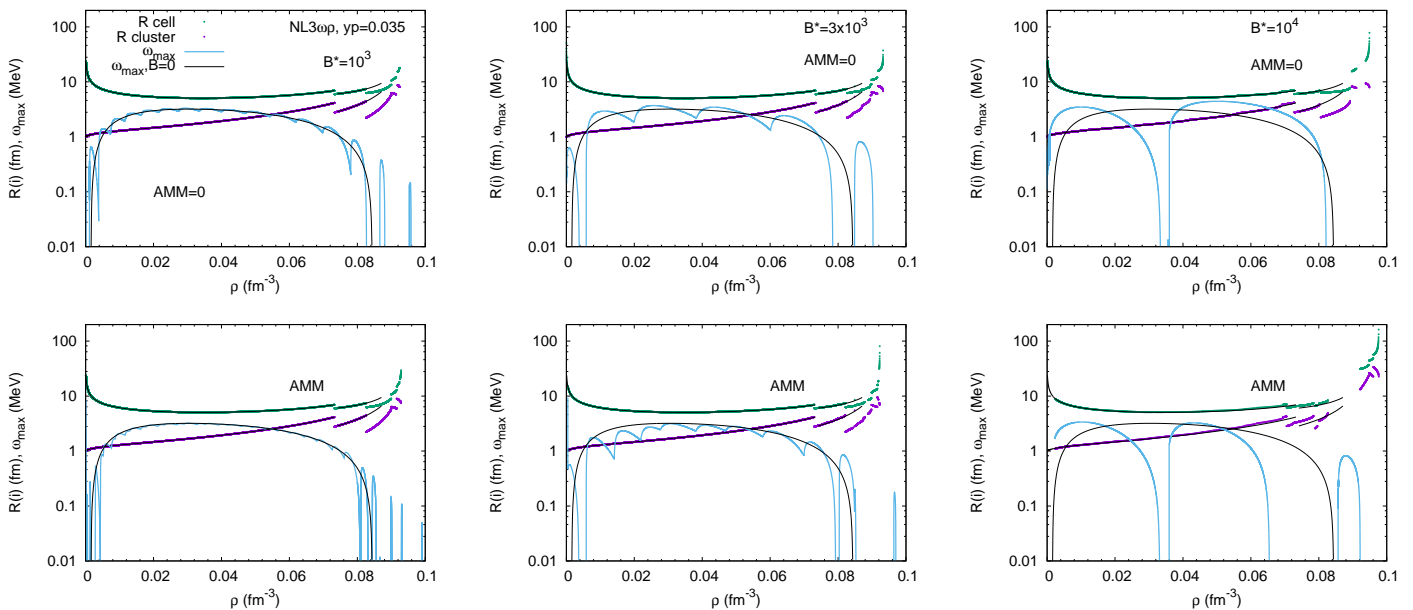


**Fig. 3.** Wigner-Seitz cell (thick green curves) and cluster radii (purple thick lines) and maximum growth rates (thin black solid lines for  $B = 0$  and light blue solid lines for finite  $B$ ) for  $B = 4.4 \times 10^{16} \text{G}$  ( $B^* = 10^3$ , left),  $B = 1.3 \times 10^{17} \text{G}$  ( $B^* = 3 \times 10^3$ , middle) and  $B = 4.4 \times 10^{17} \text{G}$  ( $B^* = 10^4$ , right), with (bottom) and without (top) AMM for the NL3 $\omega\rho$  model. The proton fraction is fixed to 0.035.

symmetry energy. In this case, the  $B = 0$  calculation predicts the existence of droplets, rods and slabs, and not only droplets. This behavior had been predicted in earlier studies [60].

In Fig. 3, the results of the calculations performed for  $B = 4.41 \times 10^{16} \text{G}$  (left),  $B = 1.3 \times 10^{17} \text{G}$  (middle), and  $B = 4.41 \times 10^{17} \text{G}$  (right) without (top) and with (bottom) AMM are shown. Thin black lines show the structure of the  $B = 0$  calculation. We also include the growth rates calculated for the same proton fraction and magnetic field intensity within a dynamical calculation [23, 25]. The effect of the magnetic field on the structure of the nonhomogeneous matter is different from what has been discussed for NL3: in the calculation without AMM, there are no well-separated nonhomogeneous regions, but there is an extension of the nonhomogeneous phase to larger densities with respect to the  $B = 0$  case; in the calculation including AMM, only for the strongest field considered a second well disconnected region of nonhomogeneous matter does appear. This behavior reflects the pattern of the dynamical spinodal unstable regions, which are smaller in extension, do not appear for densities very far from the  $B = 0$  crust-core transition, and are characterized by smaller growth rates. A second effect is the appearance of new geometries: slabs, tubes and bubbles are also present for the highest densities, as clearly seen in Fig. 4. In this figure, we identify the geometries of the clusters obtained with NL3 $\omega\rho$  without (top) and with (bottom) AMM. For  $B = 0$ , only droplets and rods are present, but for finite  $B$ , all geometries occur. For the two weaker fields, the nonhomogeneous region extends without interruption until the crust-core transition. The behavior is more irreg-

ular for the strongest field,  $B = 4.4 \times 10^{17} \text{G}$ : between the geometries, some narrow regions of homogeneous matter are present. Also, the extension of the low density region is smaller, and when including AMM, a second region of clustered matter emerges at larger densities, with slabs, tubes and bubbles.

## 5 Conclusions

The present work is an exploratory investigation of the effect of the magnetic field on the clustered matter that forms the inner crust of a neutron star. Previous investigations within a dynamical spinodal approach have suggested that the magnetic field could give origin to an extended clustered region with a crust-core transition occurring at larger densities [22, 23, 25]. Moreover, and depending on the isovector properties of the EoS, there could exist a detached nonhomogeneous region above the  $B = 0$  crust-core transition density.

Our main conclusion is that by taking the coexisting phases approach to describe clustered matter we were able to confirm the conclusions previously drawn within the dynamical spinodal calculation, in particular, that the crust-core transition occurs at larger densities. The effect of the magnetic field is not only reflected on the extension of the nonhomogeneous phase but also on the appearance of the different geometries. Taking two models with a different density dependence of the symmetry energy, it was also shown that the effect of the magnetic field is very sensitive to the behavior of the symmetry energy.

The results of the present study may help understand the violent events associated with magnetars. If the in-

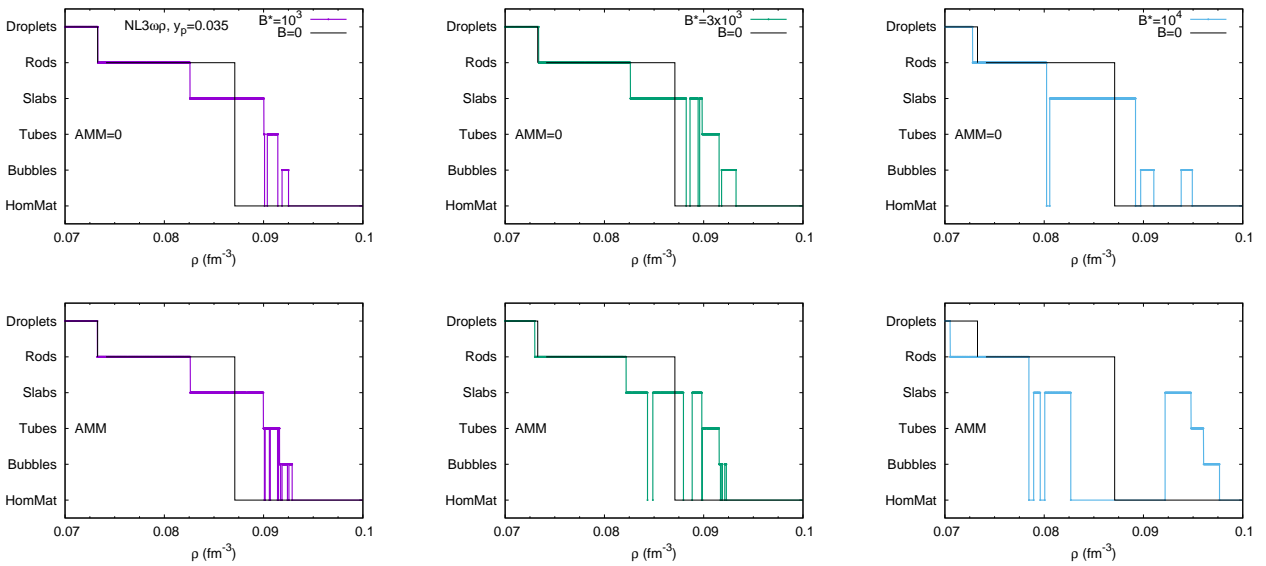


**Fig. 4.** Geometries of the clusters obtained with  $y_p=0.035$ , without (top) and with (bottom) AMM within the NL3 $\omega\rho$  model for the magnetic field intensities  $B^* = 10^3$  (left),  $B^* = 3 \times 10^3$  (middle) and  $B^* = 10^4$  (right). The thin black lines correspond the  $B = 0$  results.

ner crust structure is very sensitive to the magnetic field intensity, stresses will build as the magnetic field decays due to the change of the equilibrium structure of the star giving rise to the occurrence of fractures [61,62,33].

Our study requires further investigation within self-consistent approaches as, for instance, the Thomas-Fermi approach, that has been used to describe clusterized matter of non-magnetized [5,6,7,58,9] and magnetized matter [31,32], and imposing  $\beta$ -equilibrium.

In Ref. [32], a  $\beta$ -equilibrium calculation was carried out. The authors concluded that: larger proton fractions were obtained; no effect on the pasta structures and extension of the nonhomogeneous matter was obtained for fields  $B < 10^{17}$  G; for  $B \sim 10^{18}$  G, it was observed that the crust-core transition occurs at smaller densities and geometries that did not occur for  $B = 0$  were present, a conclusion similar to the one discussed in the last section for the strongest field considered. In Ref. [31], the calculation was performed for proton fractions of 0.1 and 0.3 within the NL3 model. Effects on the radius of the droplets, the surface tension and the crust-core transition were obtained although a systematic trend was not seen due to the possible opening of new Landau levels. In both calculations, no nonhomogeneous matter was reported above the  $B = 0$  crust-core transition possibly because this region was not investigated.

The research was developed within a RMF framework, and restricted to two models with the same isoscalar properties. We focused on the effects of a strong magnetic field on the inner crust, and in particular, the crust-core transition. Taking the  $B = 0$  proton fraction was an approximation that allowed us to understand the effect of the  $B$  field on the structure of the inner crust, independently of its effect on the proton fraction. We think that our quali-

tative findings should not depend much on the exact value of the proton fraction.

A different framework was applied to study the role of the Landau quantization of electron motion on the NS outer crust and the onset of the neutron drip in Refs. [63,64] (see also [65]). There, the authors showed, by minimizing the Gibbs energy and using atomic masses from the 2012 Atomic Mass Evaluation [66], together with masses calculated from the Brussels-Montreal Hartree-Fock-Bogoliubov nuclear mass model [67], that (1) the region of the crust where neutrons drip changes with time as the magnetic field decays; (2) the composition of the outer crust depends on the strength of the magnetic field; (3) less neutron rich matter is expected for strong magnetic fields; and (4) elastic properties as the shear modulus are affected by the magnetic field. In these works, magnetic field intensities up to  $\approx 8.8 \times 10^{16}$  G were considered. A discussion on the effects of the magnetic field on the whole, unified crust, outer and inner, should be carried out in the future.

This work was partly supported by the FCT (Portugal) Projects No. UID/FIS/04564/2019, UID/FIS/04564/2020, and POCI-01-0145-FEDER-029912, and by PHAROS COST Action CA16214. H.P. acknowledges the grant CEECIND/03092/2017 (FCT, Portugal).

## References

1. D.G. Ravenhall, C.J. Pethick, J.R. Wilson, Phys. Rev. Lett. **50**, 2066 (1983)
2. M. Hashimoto, H. Seki, M. Yamada, Prog. Theor. Phys. **71**, 320 (1984)
3. C.J. Horowitz, M.A. Pérez-García, D.K. Berry, J. Piekarewicz, Phys. Rev. C **72**, 035801 (2005)

4. G. Watanabe, T. Maruyama, K. Sato, K. Yasuoka, T. Ebisuzaki, *Physical Review Letters* **94**(3), 031101 (2005)
5. T. Maruyama, T. Tatsumi, D.N. Voskresensky, T. Tanigawa, S. Chiba, *Phys. Rev. C* **72**, 015802 (2005). DOI 10.1103/PhysRevC.72.015802
6. S.S. Avancini, D.P. Menezes, M.D. Alloy, J.R. Marinelli, M.M.W. Moraes, C. Providência, *Phys. Rev. C* **78**, 015802 (2008)
7. S.S. Avancini, S. Chiacchiera, D.P. Menezes, C. Providência, *Phys. Rev. C* **82**, 055807 (2010)
8. H. Pais, J.R. Stone, *Physical Review Letters* **109**(15), 151101 (2012)
9. S.S. Bao, J.N. Hu, Z.W. Zhang, H. Shen, *Phys. Rev. C* **90**, 045802 (2014)
10. B. Link, R.I. Epstein, J.M. Lattimer, *Phys. Rev. Lett.* **83**, 17 (1999)
11. N. Chamel, D. Page, S. Reddy, *Phys. Rev. C* **87**, 035803 (2013)
12. N. Andersson, K. Glampedakis, W.C.G. Ho, C.M. Espinoza, *Phys. Rev. Lett.* **109**, 241103 (2012)
13. J.A. Pons, D. Viganò, N. Rea, *Nature Phys.* **9**, 431 (2013)
14. S.A. Olausen, V.M. Kaspi, *Astrophys. J. Suppl.* **212**, 6 (2014). DOI 10.1088/0067-0049/212/1/6
15. <http://www.physics.mcgill.ca/~pulsar/magnetar/main.html>
16. D. Lai, S.L. Shapiro, *The Astrophysical Journal* **383**, 745 (1991)
17. C.Y. Cardall, M. Prakash, J.M. Lattimer, *The Astrophysical Journal* **554**(1), 322 (2001)
18. A.E. Broderick, M. Prakash, J.M. Lattimer, *Phys. Lett. B* **531**, 167 (2002). DOI 10.1016/S0370-2693(01)01514-3
19. D. Chatterjee, T. Elghozi, J. Novak, M. Oertel, *Mon. Not. Roy. Astron. Soc.* **447**, 3785 (2015). DOI 10.1093/mnras/stu2706
20. R.O. Gomes, H. Pais, V. Dexheimer, C. Providência, S. Schramm, *Astron. Astrophys.* **627**, A61 (2019). DOI 10.1051/0004-6361/201935310
21. I. Sengo, H. Pais, B. Franzon, C. Providência, *Phys. Rev. D* **102**(6), 063013 (2020). DOI 10.1103/PhysRevD.102.063013
22. J. Fang, H. Pais, S. Avancini, C. Providência, *Phys. Rev. C* **94**(6), 062801 (2016). DOI 10.1103/PhysRevC.94.062801
23. J. Fang, H. Pais, S. Pratapsi, S. Avancini, J. Li, C. Providência, *Phys. Rev. C* **95**(4), 045802 (2017). DOI 10.1103/PhysRevC.95.045802
24. Y.J. Chen, *Phys. Rev. C* **95**(3), 035807 (2017). DOI 10.1103/PhysRevC.95.035807
25. J. Fang, H. Pais, S. Pratapsi, C. Providência, *Phys. Rev. C* **95**(6), 062801 (2017). DOI 10.1103/PhysRevC.95.062801
26. H. Müller, B.D. Serot, *Phys. Rev. C* **52**, 2072 (1995)
27. C. Providência, L. Brito, S.S. Avancini, D.P. Menezes, P. Chomaz, *Phys. Rev. C* **73**, 025805 (2006)
28. M. Colonna, P. Chomaz, S. Ayik, *Phys. Rev. Lett.* **88**, 122701 (2002). DOI 10.1103/PhysRevLett.88.122701
29. P. Chomaz, M. Colonna, J. Randrup, *Phys. Rept.* **389**, 263 (2004). DOI 10.1016/j.physrep.2003.09.006
30. D. Chatterjee, F. Gulminelli, D.P. Menezes, *JCAP* **03**, 035 (2019). DOI 10.1088/1475-7516/2019/03/035
31. R.C.R. de Lima, S.S. Avancini, C. Providência, *Phys. Rev. C* **88**, 035804 (2013)
32. S.S. Bao, J.N. Hu, H. Shen, *Phys. Rev. C* **103**(1), 015804 (2021). DOI 10.1103/PhysRevC.103.015804
33. S.K. Lander, P. Haensel, B. Haskell, J.L. Zdunik, M. Fortin, *Mon. Not. Roy. Astron. Soc.* **503**(1), 875 (2021). DOI 10.1093/mnras/stab460
34. J. Xu, L.W. Chen, B.A. Li, H.R. Ma, *Astrophys. J.* **697**, 1549 (2009). DOI 10.1088/0004-637X/697/2/1549
35. I. Vidaña, C. Providência, A. Polls, A. Rios, *Phys. Rev. C* **80**(4), 045806 (2009). DOI 10.1103/PhysRevC.80.045806
36. C. Ducoin, J. Margueron, C. Providência, *EPL* **91**(3), 32001 (2010). DOI 10.1209/0295-5075/91/32001
37. C. Ducoin, J. Margueron, C. Providência, I. Vidana, *Phys. Rev. C* **83**, 045810 (2011)
38. W.G. Newton, M. Gearheart, B.A. Li, *Astrophys. J. Suppl.* **204**, 9 (2013). DOI 10.1088/0067-0049/204/1/9
39. H. Pais, C. Providência, *Phys. Rev. C* **94**(1), 015808 (2016)
40. B.A. Li, M. Magno, *Phys. Rev. C* **102**(4), 045807 (2020). DOI 10.1103/PhysRevC.102.045807
41. J.M. Lattimer, Y. Lim, *The Astrophysical Journal* **771**(1), 51 (2013). DOI 10.1088/0004-637x/771/1/51. URL <https://doi.org/10.1088/0004-637x/771/1/51>
42. M. Oertel, M. Hempel, T. Klähn, S. Typel, *Rev. Mod. Phys.* **89**(1), 015007 (2017)
43. D. Adhikari, et al, *Phys. Rev. Lett.* **126**, 172502 (2021). DOI 10.1103/PhysRevLett.126.172502
44. B.T. Reed, F.J. Fattoyev, C.J. Horowitz, J. Piekarewicz, *Phys. Rev. Lett.* **126**, 172503 (2021). DOI 10.1103/PhysRevLett.126.172503
45. T.G. Yue, L.W. Chen, Z. Zhang, Y. Zhou, *arXiv e-prints arXiv:2102.05267* (2021)
46. R. Essick, I. Tews, P. Landry, A. Schwenk, *arXiv e-prints arXiv:2102.10074* (2021)
47. J. Estee, et al, *Phys. Rev. Lett.* **126**, 162701 (2021). DOI 10.1103/PhysRevLett.126.162701
48. A. Broderick, M. Prakash, J.M. Lattimer, *The Astrophysical Journal* **537**(1), 351 (2000)
49. A. Rabhi, C. Providência, J.D. Providência, *Journal of Physics G: Nuclear and Particle Physics* **35**(12), 125201 (2008)
50. R.C. Duncan, *AIP Conf. Proc.* **526**, 830 (2000)
51. M.R. Frank, B.K. Jennings, G.A. Miller, *Phys. Rev. C* **54**, 920 (1996). DOI 10.1103/PhysRevC.54.920
52. G.A. Lalazissis, J. König, P. Ring, *Physical Review C* **55**(1), 540 (1997)
53. C.J. Horowitz, J. Piekarewicz, *Phys. Rev. Lett.* **86**, 5647 (2001). DOI 10.1103/PhysRevLett.86.5647. URL <https://link.aps.org/doi/10.1103/PhysRevLett.86.5647>
54. H. Pais, S. Chiacchiera, C. Providência, *Phys. Rev. C* **91**, 055801 (2015)
55. M.A. Perez-Garcia, C. Providencia, A. Rabhi, *Phys. Rev. C* **84**, 045803 (2011). DOI 10.1103/PhysRevC.84.045803
56. S.S. Avancini, C.C. Barros, Jr., D.P. Menezes, C. Providencia, *Phys. Rev. C* **82**, 025808 (2010). DOI 10.1103/PhysRevC.82.025808
57. H. Shen, H. Toki, K. Oyamatsu, K. Sumiyoshi, *Nucl. Phys. A* **637**, 435 (1998). DOI 10.1016/S0375-9474(98)00236-X
58. F. Grill, C. Providencia, S.S. Avancini, *Phys. Rev. C* **85**, 055808 (2012)
59. C. Ducoin, P. Chomaz, F. Gulminelli, *Nucl. Phys. A* **789**, 403 (2007). DOI 10.1016/j.nuclphysa.2007.03.006
60. K. Oyamatsu, K. Iida, *Phys. Rev. C* **75**, 015801 (2007). DOI 10.1103/PhysRevC.75.015801
61. S.K. Lander, *Astrophys. J. Lett.* **824**, L21 (2016). DOI 10.3847/2041-8205/824/2/L21



62. S.K. Lander, K.N. Gourgouliatos, *Mon. Not. Roy. Astron. Soc.* **486**(3), 4130 (2019). DOI 10.1093/mnras/stz1042
63. N. Chamel, R.L. Pavlov, L.M. Mihailov, C.J. Velchev, Z.K. Stoyanov, Y.D. Mutafchieva, M.D. Ivanovich, J.M. Pearson, S. Goriely, *Phys. Rev. C* **86**, 055804 (2012). DOI 10.1103/PhysRevC.86.055804
64. N. Chamel, Z.K. Stoyanov, L.M. Mihailov, Y.D. Mutafchieva, R.L. Pavlov, C.J. Velchev, *Phys. Rev. C* **91**(6), 065801 (2015). DOI 10.1103/PhysRevC.91.065801
65. D. Blaschke, N. Chamel, *Astrophys. Space Sci. Libr.* **457**, 337 (2018). DOI 10.1007/978-3-319-97616-7\_7
66. G. Audi, M. Wang, A. Wapstra, F. Kondev, M. McCormick, X. Xu, B. Pfeiffer, *Chinese Physics C* **36**(12), 1287 (2012). DOI 10.1088/1674-1137/36/12/002. URL <https://doi.org/10.1088/1674-1137/36/12/002>
67. S. Goriely, N. Chamel, J.M. Pearson, *Phys. Rev. C* **88**, 024308 (2013). DOI 10.1103/PhysRevC.88.024308. URL <https://link.aps.org/doi/10.1103/PhysRevC.88.024308>